FISEVIER

Contents lists available at ScienceDirect

# **Applied Surface Science**

journal homepage: www.elsevier.com/locate/apsusc



## Full Length Article

# Irradiation-induced amorphization of UO<sub>2</sub> films prepared by spraying-assisted combustion synthesis

Stefania Dede <sup>a,b</sup>, Khachatur V. Manukyan <sup>a,\*</sup>, Jordan M. Roach <sup>c</sup>, Ashabari Majumdar <sup>a</sup>, Peter C. Burns <sup>c,d</sup>, Ani Aprahamian <sup>a,e</sup>

- <sup>a</sup> Nuclear Science Laboratory, Department of Physics, University of Notre Dame, Notre Dame, IN 46556, USA
- <sup>b</sup> Cyclotron Institute, Texas A&M University, College Station, TX 77843, USA
- <sup>2</sup> Department of Chemistry and Biochemistry, University of Notre Dame, Notre Dame, IN 46556, USA
- d Department of Civil and Environmental Engineering and Earth Sciences, University of Notre Dame, Notre Dame, IN 46556, USA
- <sup>e</sup> A. Alikhanyan National Science Laboratory of Armenia, 2 Alikhanyan Brothers, 0036 Yerevan, Armenia

#### ARTICLE INFO

# $\begin{tabular}{ll} Keywords: \\ UO_2 thin films \\ Solution combustion synthesis \\ Ion irradiation \\ Amorphization \\ \end{tabular}$

#### ABSTRACT

Spraying-assisted combustion synthesis with uranyl nitrate — acetylacetone — 2-methoxyethanol solutions was used to prepare  $\rm UO_2$  films on an aluminum alloy substrate. The tuning of the spraying parameters and annealing temperatures allowed the preparation of  $\rm UO_2$  films with thicknesses varying from 10–300 nm and 5–10 nm  $\rm UO_2$  grain size. High-resolution electron microscopy and X-ray photoelectron spectroscopy showed that increasing the annealing temperature promotes Mg diffusion from the substrate into the films. The incorporation of Mg reduced the overall crystallinity of the films. The irradiation with  $\rm Ar^{2+}$  ions (1.7 MeV energy and a fluence of 2 ×  $\rm 10^{16}$  ions/cm²) did not degrade the quality of the films. However, the Mg content significantly influenced the irradiation-induced restructuring of the  $\rm UO_2$  films. Irradiated films with low or no Mg content exhibit high crystallinity, and the  $\rm UO_2$ /Al interfacial layer becomes highly porous. Films with higher Mg content are mostly amorphized after irradiation. The origin of irradiation-induced amorphization was related to the formation of  $\rm Mg_3\rm U_{1-y}\rm O_{2+x}$  solid solutions. Chemically complex, pore-free, and amorphous Mg-Al-O film/substrate interfacial layers enable continuous Mg diffusion during irradiation. Furthermore, the gradual increase in Mg amounts triggers irradiation-induced precipitation of a crystalline MgO-rich phase within the amorphous films.

### 1. Introduction

Uranium dioxide (UO<sub>2</sub>) is the primary nuclear fuel for most commercial power plants due to its high melting point (2865 °C), compatibility with cladding materials, as well as its high chemical and radiation stability [1–7]. Fresh UO<sub>2</sub> fuel is mildly radioactive and becomes dramatically more radioactive during reactor operations. The fuel pellets also evolve chemically, as  $^{235}\text{U}$  fission creates lighter elements, and neutron capture of  $^{238}\text{U}$  followed by  $\beta\text{-decay}$  forms transuranic elements [1,8–10].

During reactor operation, fuel undergoes considerable morphological changes [11–19]. Large thermal gradients, fission gas atoms, and neutrons create a network of defects in the micrometer-scale  $UO_2$  grains [13,20–24]. Continuous defect accumulation transforms the dense coarse-grained ( $\sim$ 10  $\mu$ m) morphology into a porous submicrometer-scale structure at the outer edges of pellets [14–16,20]. Extensive

investigations show the existence of two distinctive radiation-induced restructuring pathways: grain subdivision and recrystallization [8,9,13–16,25,26]. In the former pathway, the rearrangement of defects in large damaged grains creates new sub-boundary domains. In contrast, the latter pathway includes nucleation of new grains that grow in areas with increased concentrations of interstitials, dislocations, and stacking faults. The high operating temperatures (500-1000 °C) establish an equilibrium between defect formation and recovery. These processes make UO2 highly stable under irradiation, accommodating significant damage without amorphization [24,27,28]. The exact mechanisms governing these structural changes are unknown because of difficulties in investigating highly radioactive spent fuel [12,15,29]. Ion irradiation of thin films of UO2 or analogue (CeO2) materials is a suitable alternative for exploring such structural evolutions [28,30-34]. However, the lack of simple, safe and efficient film deposition methods impede the irradiation-induced structural investigation of UO2 at the nanoscale

Corresponding author.

E-mail address: kmanukya@nd.edu (K.V. Manukyan).



level

Solution combustion synthesis (SCS) has become an established method for preparing nanoscale materials and thin oxide films [35–43]. We recently used SCS with the spin coating to deposit thin UO $_2$  and UO $_{2.12}$  films on aluminum substrates to investigate their irradiation-induced structural changes [44,45]. The heat released during the combustion process and the subsequent annealing at 400 °C enables the preparation of polycrystalline films with ultrasmall (5–10 nm) grains of uranium oxides. The multiple deposition cycles enable the tailoring of the film thicknesses. Irradiation with 1.7 MeV Ar $^{2+}$  ions amorphized the entire UO $_2$  films at the early stages of the process (fluence below 1  $\times$  10 $^{16}$  ions/cm $^2$ ) [45]. More extended irradiation (1  $\times$  10 $^{17}$  ions/cm $^2$ ) caused recrystallization of the films. However, the atomic-scale mechanism behind the amorphization at the early stages of irradiation remains unclear.

Here we report a new preparation method of  $UO_2$  films and irradiation investigation to reveal the driving forces behind reduced radiation tolerance of nanoscale  $UO_2$ . This film preparation method combines electrospraying of uranyl nitrate — acetylacetone — 2-methoxyethanol solutions on the substrate, followed by combustion synthesis in thin solution layers triggered by short annealing. X-ray photoelectron spectroscopy (XPS) and high-resolution electron microscopy show that annealing at 350 °C yields crystalline films, and increasing the temperature decreases the overall crystallinity of the films. Probing the composition and structure of irradiated (1.7 MeV Ar $^{2+}$  ions with a total dose of 2  $\times$  10 $^{16}$  ions/cm $^2$ ) films enabled us to reveal the links between synthesis conditions and irradiation-driven structural changes, including the origin of reduced radiation tolerance of nanoscale  $UO_2$ .

#### 2. Materials and methods

#### 2.1. Preparation of thin films

Isotopically depleted uranyl nitrate hexahydrate  $(UO_2(NO_3)_2 \cdot 6H_2O)$ , International Bio-Analytical Industries,  $\geq 98.0$  %) was dissolved in 2-methoxyethanol  $(C_3H_8O_2)$ , Alfa Aesar, 99 %). Caution:  $UO_2(NO_3)_2 \cdot 6H_2O$  is a highly toxic compound and contains radioactive <sup>238</sup>U, an alpha particle emitter. Only trained personnel should handle this compound within a licensed facility. Then, acetylacetone  $(C_5H_8O_2)$ , TCI, >99.0%) fuel was added to obtain a solution with a 0.5 M ratio of  $C_5H_8O_2$  to  $UO_2(NO_3)_2$ .

Fig. 1 shows the schematic representation of the electrospray deposition setup. It consists of a syringe pump (KDS 100 Legacy Single Syringe Infusion Pump), an airtight syringe (Hamilton gas-tight syringe,  $500~\mu$ l), a high voltage power supply, a stainless steel spraying nozzle

with an inner diameter of 0.25 mm, and a hot plate (Cimarec+TM Hotplate Series). The solution is forced through the nozzle by high voltage (15 kV) spraying on a mirror-finished aluminum alloy (6061, with impurities: Cr 0.04–0.35 %, Cu 0.15–0.4 %, Fe <0.7 %, Mn <0.15 %, Si 0.4–0.8 %, Ti <0.15 %, Zn <0.25 %, and Mg 0.8–1.2 wt%).

The aluminum substrates were annealed in air at 300 °C for 30 min, followed by ozone cleaning for 20 min before the deposition to improve substrate wettability. After spraying, the samples were placed in a preheated furnace to initiate the combustion in the solution layers. The spraying time was varied from 15 to 120 min with the flow rate changing from 3 to 30  $\mu$ l/h. Other variable parameters include uranyl nitrate concentration (0.10–1 M), the hot plate temperature during spraying (50 °C to 200 °C), and the annealing temperature (350 °C to 550 °C) and duration (20 to 90 min).

The irradiation of selected samples (30 min spraying time, 30  $\mu l/h$  solutions flow rate, annealed at 350 °C and 550 °C for 20 min) with an Ar^2+ beam (energy of 1.7 MeV and fluence of 2  $\times$  10^{16} ions/cm²) was conducted using the single-ended accelerator (5U) at the Nuclear Science Laboratory at the University of Notre Dame [45]. An ion range (~1,000 nm) and damage profile were calculated using the Stopping and Range of Ions in Matter (SRIM). These calculations show that nearly 100 % of the Ar²+ beam passes through the UO2 film and stops in the Al substrate (Fig. 1S). The irradiation was performed at normal incidence over  $\sim 1.3~\text{cm}^2$  area with an ion flux of  $\sim \! 10^{12}~\text{ion/cm}^2/\text{s}$ . A water circulation system cooled the Al substrate at 15 °C to minimize beam heating effects during irradiation.

#### 2.2. Characterization of thin films

An Alpha Suite Spectrometer (ORTEC) with an ULTRA-AS ion-implanted silicon detector was used to measure four uranium isotopes in the deposited films. This detector has  $\sim 100~\mu m$  active depth, an active area of 900 mm², and a resolution of 29 keV FWHM at 5.486 MeV. A mixed ( $^{148}\text{Gd}$  and  $^{241}\text{Am}$ ) alpha source was used for the energy calibration. The solid angle was determined using the SACALC software [45]. All the measurements were performed under vacuum ( $\sim \! 10~Pa$ ). The total content of the four uranium isotopes ( $^{238}\text{U},~^{235}\text{U},~^{236}\text{U},~\text{and}~^{234}\text{U}$ ) was calculated by applying the branching ratio correction of alpha particles for each specific decay chain.

X-ray photoelectron spectroscopy (XPS) was used to analyze the near-surface composition and chemical states of the films. The XPS samples (2  $\times$  2 mm) were prepared from the original samples using a metal shear cutter and mounted on the sample holder. A PHI VersaProbe II spectrometer with an Al K X-ray source operating at 1486.6 eV with a 90° take-off angle was employed. Analysis of the valence level (O 2p and

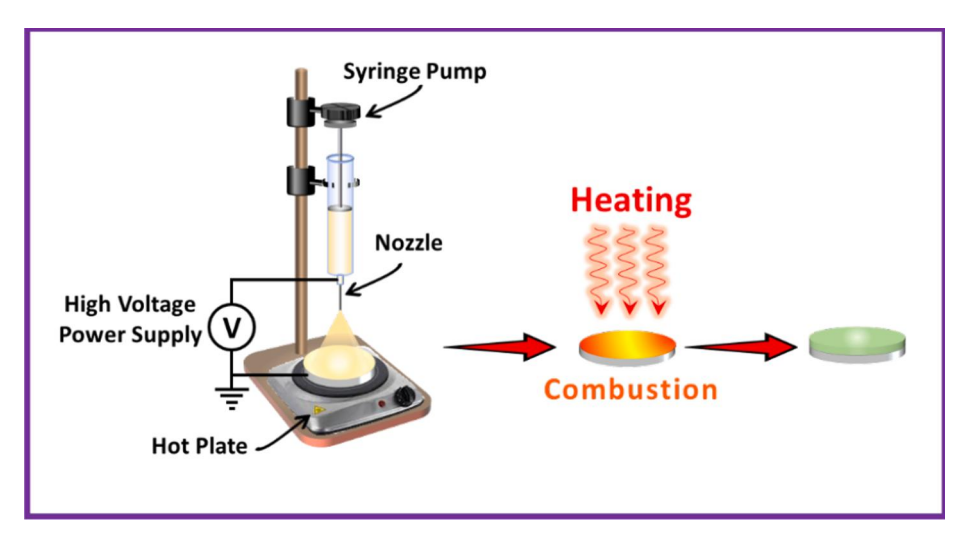


Fig. 1. Schematic representation of UO<sub>2</sub> film deposition on Al substrate.

U 5f) and core (O 1 s, U 4f, Mg 1 s) photoelectrons was conducted under  $10^{-9}$  mbar pressure. Ar $^+$  etching at an accelerating voltage of 2 kV and current density of  $25 \,\mu\text{A/cm}^2$  was used, with a duration from 180 to 540 sec, to analyze the chemical states of films at different depths. The binding energies were measured relative to the U<sup>4+</sup> binding energy (380.2 eV). Fifteen to twenty scans were obtained and averaged for each electronic transition while ten passes were used for the survey scan. The electron pass energy was set at 23.500 eV for each element and 187.85 eV for the survey scan. The background was subtracted using the Shirley method [46]. CasaXPS software was used to analyze the spectra [47].

Calculation of the oxygen coefficient  $k_0=2+x$  for  $UO_{2+x}$  using an approach based on the core level  $U4f_{7/2}/O1s$  intensity ratio produced unreasonable  $k_0$  values (from 3 to 5) and could not be used for the oxidation state calculation, as was previously shown by Teterin et al. [7,48-50]. Instead, it was determined using the ratio  $U5f/U4f_{7/2}$  (without satellite peaks) based on the following equation [7,31]:

$$\frac{U5f}{U4f_{7/2}} = I_1 = 5.366k_0^{-7.173} \tag{1}$$

The fractions  $\nu$  ( $\mathbf{U}^{n+}$ ) of the uranium ions in different oxidation states were calculated by using Eqs. (2)–(4):

$$\nu_1(U^{4+}) = I_3/0.0383 \tag{2}$$

$$\nu_2(U^{5+}) = 2(I_2 - I_1)/0.0383 \tag{3}$$

$$\nu_3(U^{6+}) = (0.0383 - I_2)/0.0383 \tag{4}$$

where the  $I_2$  and  $I_3$  coefficients were determined by the following equations:

$$I_2 = -0.0383k_0 + 0.1149 (5)$$

$$I_3 = I_2 - 2(I_2 - I_1) = 2I_1 - I_2$$
(6)

An Orbis (EDAX) X-ray fluorescence (XRF) analyzer with a Rh X-ray tube, poly-capillary optics, and an 80 mm  $^2$  Si(Li) drift detector was utilized to determine the elemental composition and to characterize the overall uniformity of the films deposited on Al substrates. The X-ray beam parameters (40 kV, 400  $\mu\text{Amp}, 0.03$  mm spot size) were consistent throughout the measurements with a 100 ms per point rate.

Scanning electron microscopy (SEM) was used to investigate the surface morphology of the films. Helios Nanolab 600 (Thermo Fisher Scientific) with a dual electron/ion beam system was used both for secondary-electron SEM imaging and preparation of thin (50-100 nm) slices for cross-sectional transmission electron microscopy (TEM) measurements [30,51,52]. For TEM sample preparation, a carbon layer (1  $\mu m$  thick) in a 10  $\mu m \times 0.5 \mu m$  rectangular area was deposited onto the selected area of films. Next, ~1 μm deep trenches with a 52° base angle were milled on both sides of the carbon layer with an accelerating voltage of 5 keV and a milling current of 27 nA. Then, the slice was lifted from the sample and polished to a ~ 70 nm thickness under an accelerating voltage of 5 keV and a milling current of 700 pA to produce clean cross-section samples for TEM images without milling artifacts. The morphology and structure of these slices were investigated using a Titan-300 (FEI) microscope with a resolution of 0.136 nm in scanning TEM mode and about 0.1 nm information limit in high-resolution TEM mode. The Titan was equipped with an energy-dispersive X-ray spectroscopy (EDS, Oxford Inca) system containing a Si(Li) detector with an energy resolution of ~ 130 eV at 5.9 keV. Selected area electron diffraction patterns of UO2 films were acquired by an aperture with a diameter of 100 nm. The ring-type diffraction patterns were radially averaged to obtain a distribution profile as a function of the scattering vector (S =  $2\sin\theta/\lambda$ , where  $\lambda$  is the de Broglie wavelength, and  $\theta$  is the scattering angle).

#### 3. Results

#### 3.1. Thin-film deposition

The effect of uranyl nitrate concentration in the reactive solution was initially explored. Five solutions with varying uranium concentrations (0.1 to 1 M) were sprayed with a flow rate of 20 µl/h for 30 min on Al substrates at a 50 °C hot plate temperature, and were then annealed at 450 °C for 20 min. The total number of uranium atoms (<sup>238</sup>U, <sup>235</sup>U, <sup>236</sup>U, and <sup>234</sup>U) measured by alpha spectroscopy shows a linear increase with the concentration of uranyl nitrate in the sprayed solution until a concentration of  $\sim 0.5\ \text{M}$  was reached (Fig. 2A). A further increase in concentration led to less significant increases and an eventual saturation of the uranium amount, presumably due to the increasing viscosity of the solution. Therefore, a reactive solution with 0.25 M concentration was selected to test the effects of other parameters. Fig. 2B shows a direct and linear relationship between solution flow rate and uranium amount in the deposited films. Note that the spraying time in this series was fixed at 30 min. Similar results were also observed for the different spraying time series (Fig. 2C). Fig. 2D shows that hot plate temperature does not influence the amount of deposited uranium on the substrates, while it does impact the microstructures of the films.

SEM images of a film deposited at 50 °C and annealed at 450 °C indicate a smooth and uniform coverage of the UO $_2$  layer on the substrate (Fig. 3A). Slight heating during the deposition helps spread the solution and produces coatings without visible surface roughness. The increase of the hot plate temperature to 100 °C forms cavities of varying sizes (0.1–0.5  $\mu$ m) (Fig. 3B). A magnified view of these features (inset in Fig. 3B) reveals a porous microstructure with an average pore diameter of 250 nm. Further increase in the hot plate temperature (200 °C) decreases the size of these cavities (Fig. 3C). The porosity of the layer slightly decreases as well. The higher substrate temperatures accelerate the solvent evaporation and create non-uniform porous microstructures.

Fig. 3D shows a typical single-point XRF spectrum acquired from a film, where the composition of the Al alloys substrate is confirmed, along with the presence of a uranium characteristic M X-ray line (3.17 keV). Fig. 3E and F illustrate the color-coded intensity distributions for U M and Al K (1.49 keV) lines across the sample. These images show that the uranium layer is uniformly distributed over the entire coated area, while the intensity of the characteristic peak for aluminum is reduced.

#### 3.2. Structural features of thin films

The effects of annealing temperature (350 °C to 550 °C) for durations lasting 20–90 min were investigated relative to the morphology and structure of the films (Fig. 4). At 350 °C, the UO $_2$  layer exhibits small (2–5 nm) pores (Fig. 4A), while high-resolution TEM images at higher magnification show several grains with different orientations and a grain with interplanar spacings of 0.308  $\pm$  0.002 nm corresponding to a (111) diffraction plane. Electron diffraction patterns show well-defined Debye–Scherrer rings corresponding to the fluorite-type cubic structure of UO $_2$  (Fig. 4A, right panel). The diffraction profile shows relatively narrow peaks, indicating that the films indeed have a highly crystalline structure.

Fig. 4B shows that increasing the annealing temperature to 450  $^{\circ}$ C does not change the morphology of the films, which exhibit similarly sized pores as the film prepared at 350  $^{\circ}$ C. However, high-resolution TEM images display grains with well-defined boundaries and some areas with disordered structures. Moreover, the intensity of the diffraction lines slightly decreases. Note that the increase in annealing time from 20 to 90 min at 450  $^{\circ}$ C further reduces film crystallinity and pore sizes (see Fig. 2S).

The films prepared at 550 °C are uniform in thickness with significantly less porosity (Fig. 4C). However, the grains have smaller diameters than those produced at lower temperatures, and the films contain larger areas of disordered structures. Finally, the diffraction

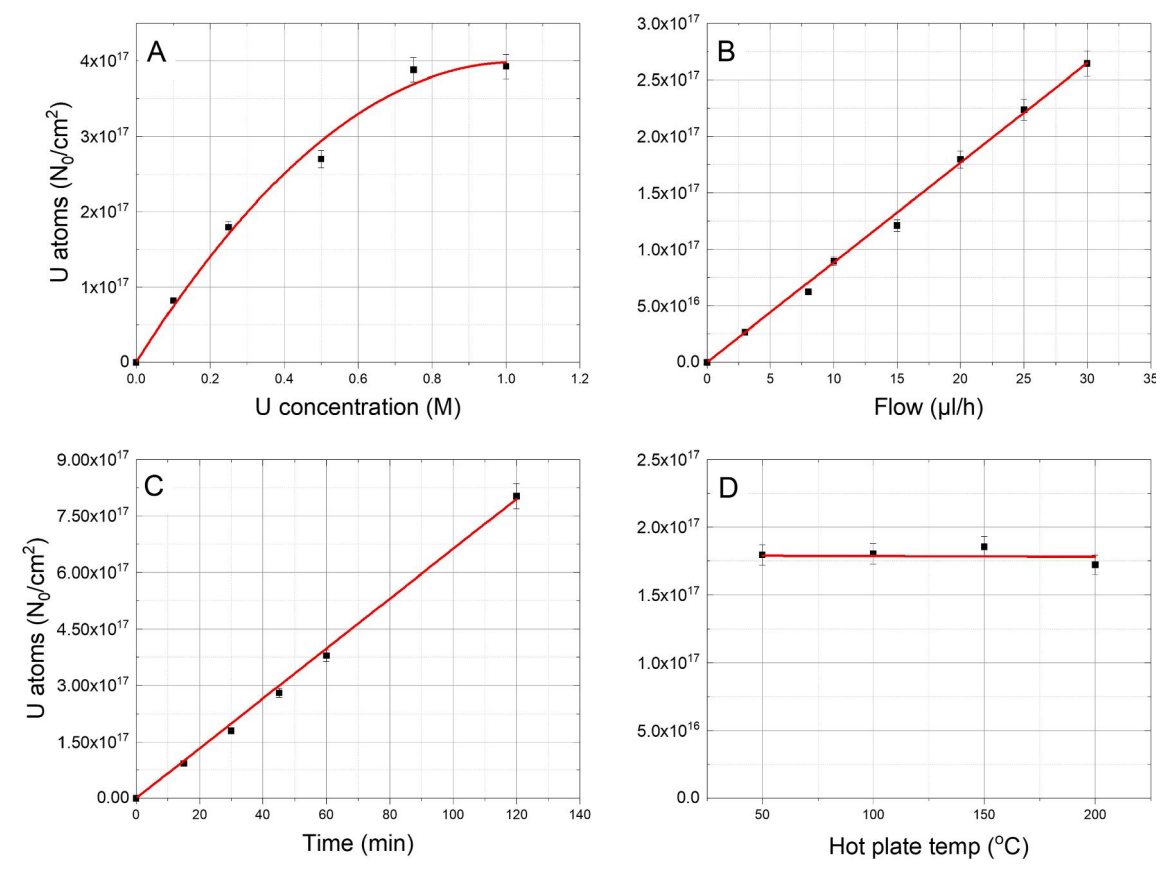


Fig. 2. Uranium amount in the samples vs the uranyl nitrate concentration in solution (A), the flow rate (B), the spraying time (C), and the hot plate temperature prior to annealing (D) at 450 °C for 20 min.

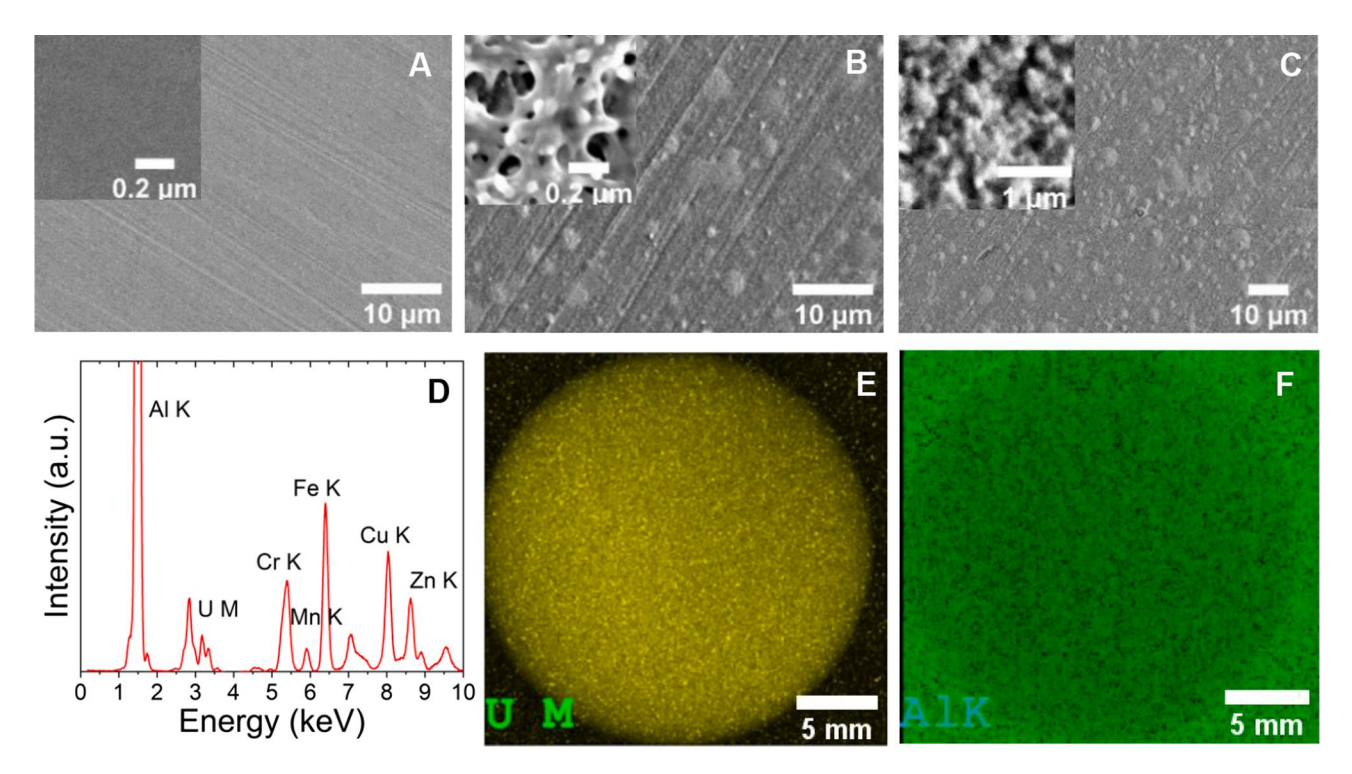


Fig. 3. SEM images of UO<sub>2</sub> layers deposited on Al at 50 °C (A), 100 °C (B) and 200 °C (C) hot plate temperatures, single-point XRF spectrum (D), intensity distributions for U M (E) and Al K (F) characteristic X-ray lines across the sample. 30-minute spraying of solution (0.25 M concentration) with 20  $\mu$ l/h flow rate and annealed at 450 °C for 20 min.

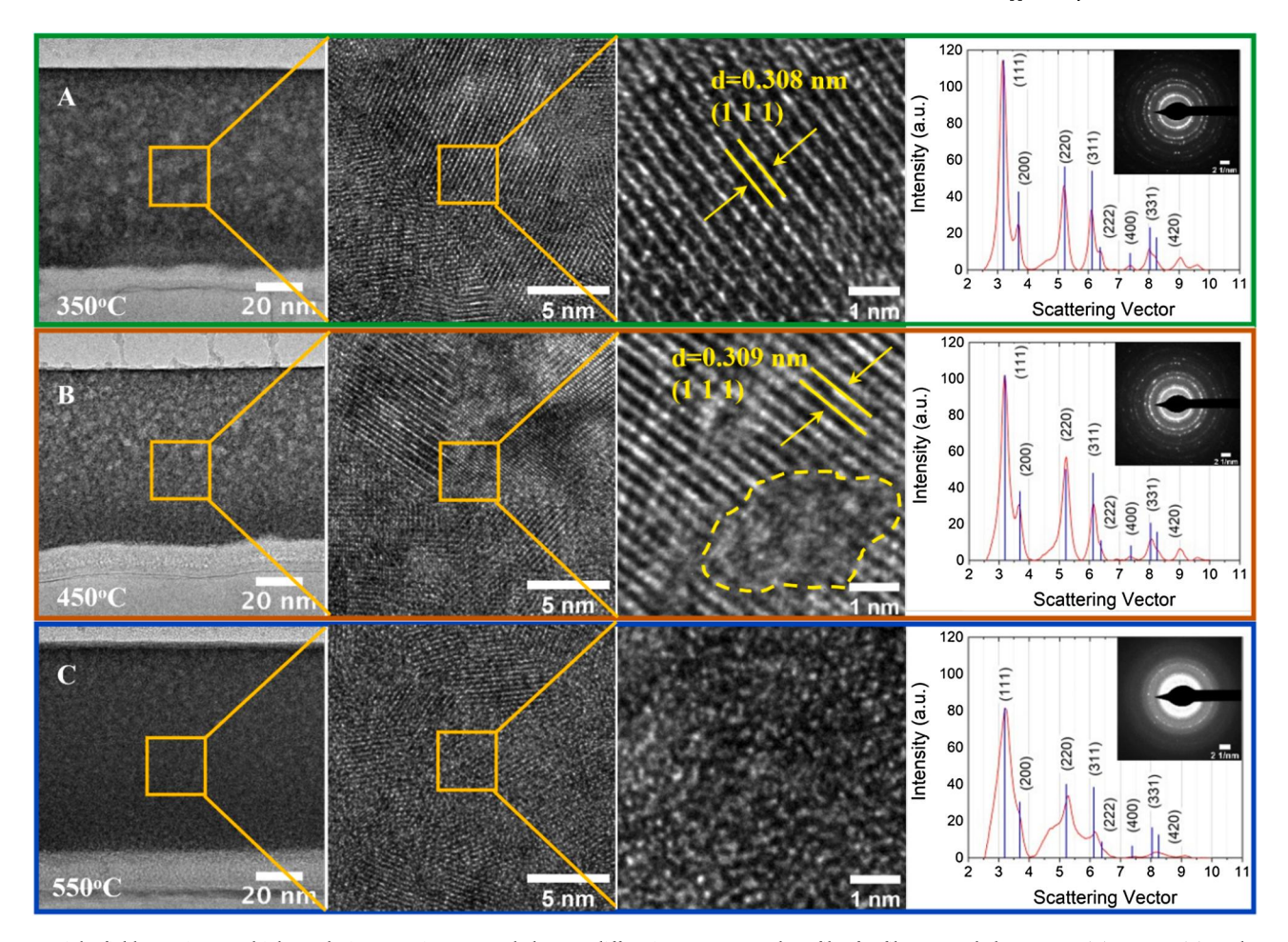


Fig. 4. Bright-field TEM images, high-resolution TEM images, and electron diffraction patterns and profiles for films annealed at 350  $^{\circ}$ C (A), 450  $^{\circ}$ C (B), and 550  $^{\circ}$ C (C) for 20 min. All samples were made with 30-minute spraying of 0.25 M solutions at a flow rate of 20  $\mu$ l/h.

profile contains broad lines, and several adjacent peaks (such as (200) and (311)) are unresolved due to peak broadening.

The images and electron diffraction analyses in Fig. 4 and 2S show that increasing the annealing time and temperature decreases the crystallinity of UO<sub>2</sub> films with a simultaneous decrease in porosity. A crosssectional EDS analysis was conducted to investigate the origin of the observed transition. The amount of Mg in the films (and at the film/ substrate interface) correlates with the annealing temperature (Fig. 5 and 3S). The UO<sub>2</sub>/Al interface of the film prepared at 350 °C contains a significant amount of Mg. However, there is much less Mg throughout the remainder of the film (Fig. 5A and Fig. 3S), indicating no significant migration. At 450 °C (20 min of annealing), the Mg is mainly localized within the UO<sub>2</sub>/Al interface (Fig. 5B and Fig. 3S). Increasing the annealing duration (90 min at 450  $^{\circ}$ C) or temperature (550  $^{\circ}$ C) results in diffusion of Mg into the UO<sub>2</sub> layer (Fig. 5C, 3S, and 4S). The Al alloy used as a substrate contains ~ 1.2 wt% Mg. Therefore, higher annealing temperatures or prolonged heating facilitate the diffusion of Mg from the bulk alloy to the interface and eventually into the deposited film. The correlation between the Mg content and the amount of disorder areas suggests that Mg incorporation reduces the overall crystallinity of UO2 films.

#### 3.3. Oxidation states of films

A layer-by-layer XPS analysis was conducted to gain insight into the effects of Mg diffusion on film crystallinity and oxidation states. In these experiments,  $\mathrm{Ar}^+$  etching with varying durations (30 to 540 sec) was used to remove  $\mathrm{UO}_2$  layers and analyze the films at different depths

(estimated to be from 3.5 to 65 nm). The fitting of the uranium core electron spectra was based on the binding energies of the spin–orbit splitting U 4f lines for U(IV) at 379.8 – 380.1 eV, U(V) at  $\sim$  380.0 eV, and U(VI) at  $\sim$  380 – 382 eV, as well as the positions of the satellite peaks  $\sim$  7.1 eV,  $\sim$ 7.8 eV and  $\sim$  3.5 eV above the spin–orbit splitting U4f peaks, respectively [53]. The energy separation of the U 4f<sub>7/2</sub> and U 4f<sub>5/2</sub> was constant throughout the different data sets (10.8 eV) and consistent with the values reported in the literature [7,31].

Fig. 6 shows XPS spectra acquired for different  $Ar^+$  etching times for films prepared at 350 °C. After 30 sec of etching, the U 4f peaks are less prominent than after more extended etching, and the satellite peaks are not visible. The intensities of the peaks increase with the etching time, and the satellites become well-defined (Fig. 6A). A "metallic" or reduced uranium (valence states lower than IV) component at 378.8 eV also became evident with increased etching time.

For the valence electron spectra (Fig. 6B), the separation between the U 5f (1.48 eV) and the outer valance molecular orbitals (OVMO) (4.4 eV) is not as sharp after 30 s of etching time in comparison to more extended etching times. The U 5f peak shifts from 1.78 to 1.48 eV in the spectra acquired with 180 and 540 s etching times. The peak broadening also accompanies this shift due to the increase of the  $\rm U^{4+}$  concentration (Table 1).

The intensities of the core level oxygen peaks (530.1 eV) also change with etching time, while the OH (531 eV) and the  $CO_3^{2-}$  (532.1 eV) components appear unchanged throughout the sample (Fig. 6C). The presence of these surface groups is attributed to the porous nature of the deposited layers obtained in ambient air. Mg was not detected in the sample prepared at 350 °C, consistent with the EDS results (Fig. 3S).

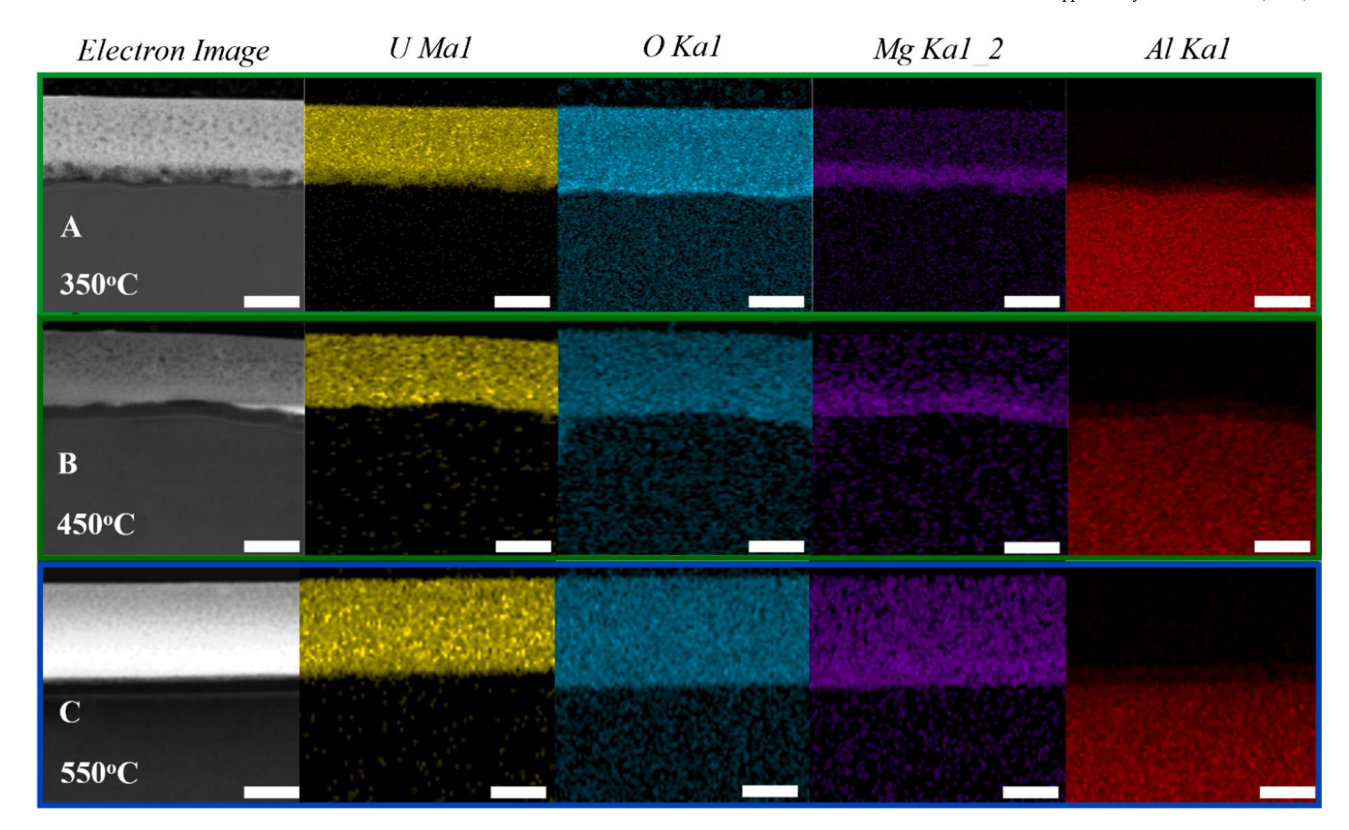


Fig. 5. EDS elemental maps for samples annealed at 350 °C (A), 450 °C (B) and 550 °C (C) for 20 min. The scale bar is 100 nm for all the figures.

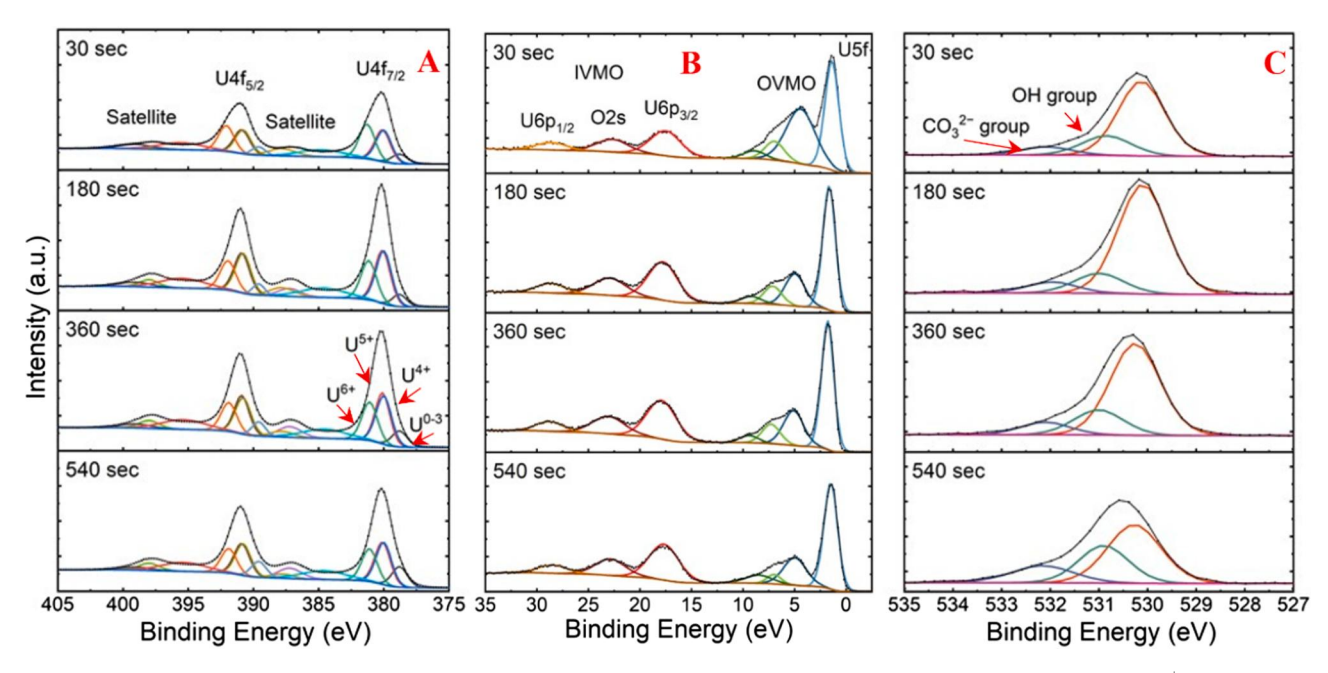


Fig. 6. XPS spectra for the U 4f core (A), U 5f valence (B), and O1s core (C) electrons for films prepared at 350 °C with different Ar<sup>+</sup> etching times.

Similar data were obtained for the samples prepared at 450 °C (Fig. 5S) and 550 °C (Fig. 7). The intensities of the U 4f peaks increase with etching time, and the satellites become more prominent, in addition to the "metallic" uranium (378.8 eV) component (Fig. 7A). For the valance level electrons (Fig. 7B), the same separation issues exist between the U 5f peak (0.90 eV) and the OVMO (3.62 eV) peaks, followed by a shift towards lower binding energies. The binding energies for the U 5f ( $\sim$ 1.53 eV) and the OVMO ( $\sim$ 4.70 eV) remain constant for longer etching times.

The main differences between the XPS spectra of samples obtained at 350 °C and higher temperatures are the oxygen peaks. Fig. 7C shows that after 30 sec of etching, the binding energy for the O 1 s peak shifts from 530.1 eV to 529.7 eV, while the peaks are centered at 530.4 eV for longer etching times. The film prepared at 450 °C shows no Mg 1 s peaks for the 30 sec etching time (Fig. 6S A). Longer (180 – 540 sec) etching times reveal small Mg 1 s peaks resulting in  $\sim$  0.18 at. % of Mg. The films obtained at 550 °C contain considerably higher Mg (Fig. 6S B) with visible peaks even for the 30 sec etching time.

Table 1 Oxygen coefficients  $(k_0)$ , oxidation states of U and Mg concentration.

Annealing temperature	Etching time (sec)	$I_1$	$k_0$	$I_2$	$I_3$	Fractions of $\mathit{U}^{n+}$ ions, %			Mg (At.%)
						U <sup>4+</sup>	U <sup>5+</sup>	U <sup>6+</sup>	
350 °C	180	0.026	2.101	0.034	0.018	46 ± 3	44 ± 3	$10\pm1$	=
	360	0.027	2.092	0.035	0.019	$50\pm3$	$41\pm3$	$9\pm1$	_
	540	0.028	2.085	0.035	0.020	$53 \pm 3$	$39\pm3$	$8\pm1$	_
450 °C	180	0.028	2.077	0.035	0.021	$56 \pm 3$	$36\pm3$	$8\pm1$	0.14
	360	0.029	2.068	0.036	0.023	$60 \pm 3$	$34 \pm 3$	$7\pm1$	0.15
	540	0.030	2.061	0.036	0.024	$62 \pm 3$	$31\pm3$	$6\pm1$	0.18
550 °C	180	0.029	2.070	0.036	0.023	$59 \pm 3$	$34\pm3$	$7\pm1$	4.31
	360	0.030	2.063	0.036	0.024	$62\pm3$	$32\pm3$	$6\pm1$	4.20
	540	0.030	2.063	0.036	0.024	$62\pm3$	$32\pm3$	$6\pm1$	5.69

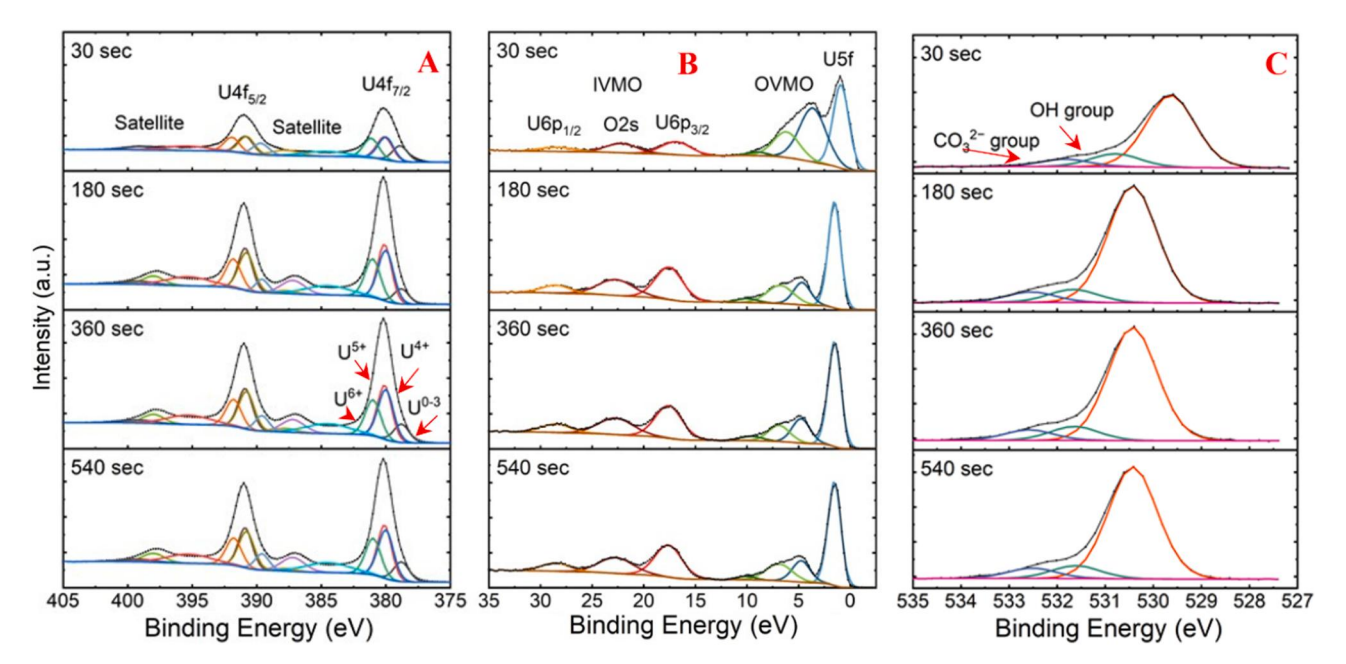


Fig. 7. XPS spectra of the U 4f core (A), U 5f valence (B) and O1s core (C) electrons for films prepared at 550 °C with different Ar<sup>+</sup> etching times.

The calculated At.% of the Mg content are included in Table 1, showing a gradual increase in Mg from 0.73 At.% (30  $\sec$  of etching) to 5.69 At.% (540  $\sec$  of etching) for 550 °C annealing temperature. Table 1 also summarizes the oxidation states of U and the  $k_0$  coefficient for the films prepared at different temperatures determined by the U5f /U4f<sub>7/2</sub> ratio [31]. All three samples exhibit the same trend for  $k_0$ , which decreases with the etching duration. At the same time, the amount of U with 4 + oxidation state increases, while the amount of the 5 + and the 6 + decreases. This trend correlates well with increasing Mg concentration closer to the film/substrate interface.

#### 3.4. Irradiation

The UO $_2$  films prepared at different temperatures were characterized by  $\alpha$  particle spectroscopy to determine the uranium content before and after irradiation. Fig. 8A shows signals reflective of the  $^{238}$ U,  $^{235}$ U,  $^{236}$ U, and  $^{234}$ U isotope content for the pristine samples prepared at 350 °C before and after irradiation. The number of each isotope per cm $^2$  was determined from these spectra, indicating no loss of material after irradiation (Table 1S). Despite the material conservation, irradiation considerably changes the morphology of the films. The UO $_2$ /Al interfacial layer becomes porous, while the porosity of the UO $_2$  layers is significantly reduced (Fig. 8A). However, the sizes of the UO $_2$  grains increase during irradiation. An electron diffraction pattern (Fig. 8A) shows scattered bright spots instead of the ring patterns of the pristine samples, indicating enhanced crystallinity (Fig. 4A). The improved

crystallinity can also be seen on high-resolution TEM images for the  $UO_2$  film and film/substrate interface (Fig. 8A).

The  $\alpha$  particle spectra from the samples prepared at 550 °C before and after ion irradiation are similar (Fig. 8B). The number of uranium isotopes (Table 2S) determined from these spectra also show that irradiation does not lead to sputtering degradation and material losses. TEM imaging revealed no changes in the film/substrate interface (Fig. 8B). However, in contrast to the 350 °C microstructure, nearly the entire film is amorphized, as shown by the electron diffraction pattern (Fig. 8B) and the high-resolution TEM image (Fig. 8B). A thin discontinuous crystalline sublayer forms closer to the surface of the UO<sub>2</sub> films with a significantly high Mg content (Fig. 7S). Directly measured lattice spacings on high-resolution TEM images show that this structure is MgO (Fig. 8B).

#### 4. Discussion

This work reports a rapid and simple method for the preparation of thin  $UO_2$  films. Combining SCS with electrospraying allows the deposition of uniform films at low temperatures. This approach enables the preparation of films with efficiency of the uranium precursors compared to the spin-coating assisted combustion method reported in previous works [44,45]. The high material collection efficiency (MCE) makes spraying-assisted SCS ideal for fabricating thin oxide films of highly radioactive and expensive oxides of transuranic elements.

The method reported herein also presents multiple advantages over polymer-assisted deposition (PAD) [54–56], electrodeposition [57–60],

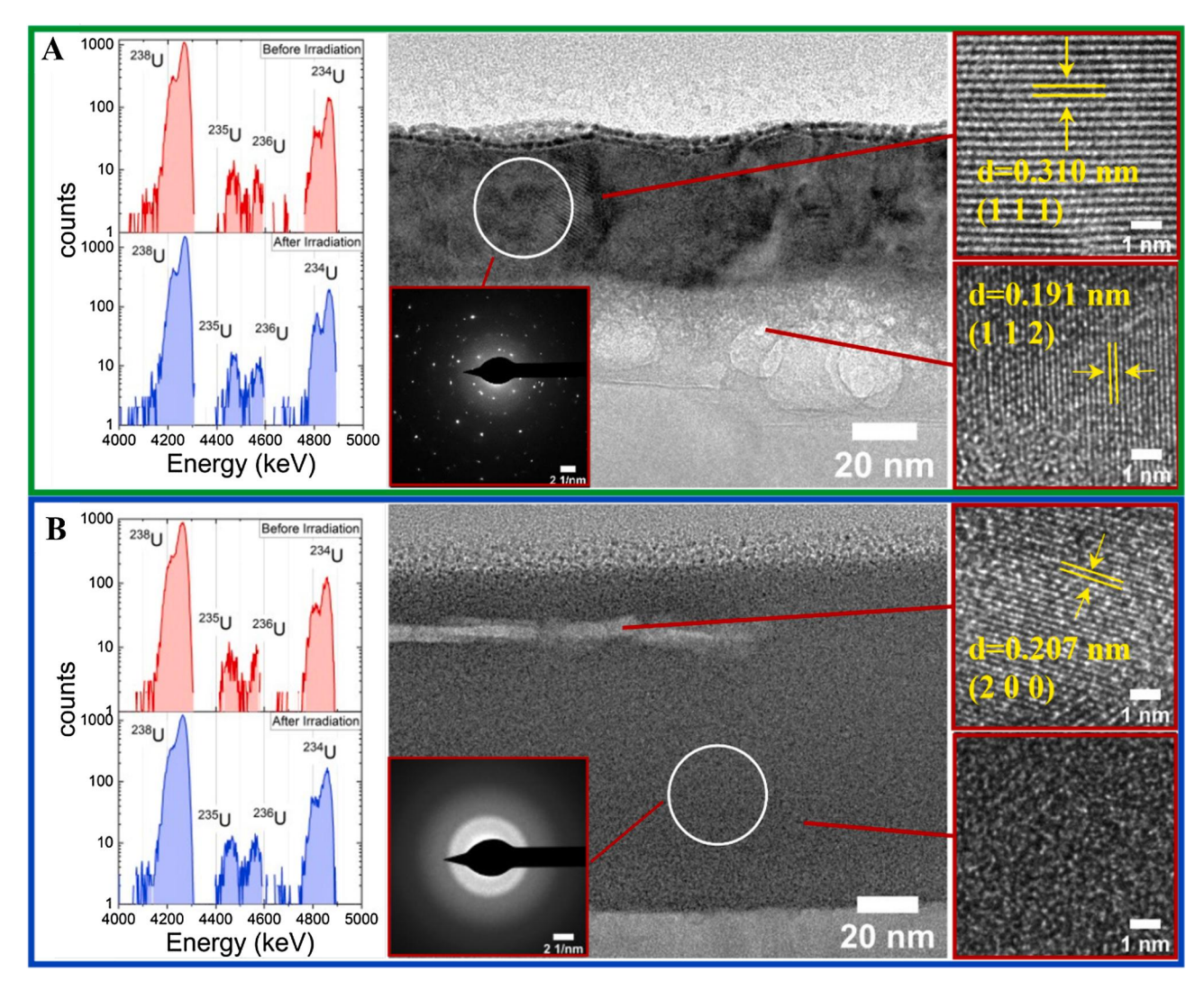


Fig. 8. Alpha particle emission spectra for samples prepared at 350 °C (A) and 550 °C (B) before and after irradiation, as well as TEM, high-resolution TEM images, and electron diffraction patterns of irradiated films.

magnetron sputtering [61–65], and chemical vapor deposition (CVD) of UO<sub>2</sub> films [66–68]. For example, PAD relies on spin coating of substrates with water-based polymer solutions containing metal salt, followed by slow annealing to  $\sim900~^\circ\text{C}$  to oxidize organic residues and obtain a crystalline UO<sub>2</sub> film. PAD produces homogenous films by repeating the spin coating and annealing cycles. However, the MCE is only  $\sim30~\%$ . In contrast, electrodeposition is highly efficient (MCE ranges from 80 to 98 %). The setup for electrodeposition is simple, and the duration of the process is reasonably short. However, the most crucial disadvantage of this method is the low adherence of the deposited material to the substrates and the high levels of impurities in the films. The uniformity of the films is also low. The deposited layers usually result in microscopic "islands" rather than thin uniform layers.

The magnetron sputtering method allows the production of epitaxial thin ( $\sim$ 100 nm) uranium oxide films. However, this method requires extensive and dedicated ultra-high vacuum instrumentation and specifically prepared metallic uranium source material. The composition and U/O ratio of films are tuned by changing the oxygen pressure in the deposition chamber. The CVD method uses volatile and highly toxic metal–organic compounds. The control over the stoichiometry in the CVD process is challenging, and other uranium oxides form as minor phases in addition to UO<sub>2</sub>.

 $\rm UO_2$  films prepared and reported in this work result in uniform coverage over areas of  $\sim 5~\rm cm^2$ , tunable thicknesses, excellent thickness

uniformity, and a consistent U/O ratio. The films are also robust and stable under high-energy ion irradiations. The annealing temperatures enable the tuning of film crystallinity. At 350 °C, the UO<sub>2</sub> films are highly crystalline, while the increase in temperature to 550 °C or prolonged annealing at 450 °C leads to the formation of areas without longrange order. Such unusual structural changes correlate well with gradual diffusion of Mg from the alloy substrate into the film/substrate interface and subsequently into the UO<sub>2</sub> films. Non-coated aluminum alloys have a thin (~5 nm) Al<sub>2</sub>O<sub>3</sub> layer with a small quantity of Mg (1–2 At.%). The low pH (~2) value of the reactive solution accelerates the oxidative leaching of Mg from the bulk of the alloy into the interfacial layer.

Prior work suggested that substitutional types of  $Mg_yU_{1-y}O_{2\pm x}$  ( $0 \le y \le 0.33$ ) solid solutions form in the U-Mg-O system at 800 °C [69–72]. Our XPS results show slight changes in the surface compositions of the deposited oxide layer and the presence of a "metallic" component. Cross-sectional EDS analysis also shows sizable increases of Mg in thin films prepared at 550 °C. Ultra-small UO<sub>2</sub> grains likely facilitate the formation of a  $Mg_yU_{1-y}O_{2\pm x}$  solid solution at much lower temperatures than micrometer-scale grains reported earlier [69]. However, the solid solution appears amorphous due to the relatively low temperatures.

To characterize the irradiation stability of the  $UO_2$  films, we used relatively heavy  $Ar^{2+}$  ions to create uniformly distributed atomic defects without causing bubbles or dislocation loops (see Fig. 1S). Irradiation of the films prepared at 550 °C further facilitates the diffusion of Mg into

the  $UO_2$  layer. Ultrasmall  $UO_2$  grain sizes, ion flux, and an increasing amount of solid solution create a primarily amorphous film with a crystalline discontinuous MgO-rich sub-layer. Chemically complex MgAl-O film/substrate interfacial layers in samples prepared at 550 °C remain amorphous and pore-free during irradiations, thus providing a continuous supply of Mg throughout the irradiation.

It is noteworthy that the crystallinity of films deposited at 350 °C improves after irradiation. TEM imaging and electron diffraction patterns indicate that a significant UO2 grain growth occurs without a preferential direction. The grain coarsening takes place in all directions. In our irradiation experiment, the samples were cooled by circulating water to minimize possible beam-induced heating during irradiation. Therefore, we assume that irradiation-induced coarsening is governed by ballistic mixing at disorder areas such as grain boundaries. The growth process occurs even near ambient temperatures due to the ultrasmall grain and high grain boundary area. The structural refinement in these regions leads to ordering at the interface of grains and possibly transitioning from asymmetric to symmetric grain boundaries to minimize the system's overall energy. TEM imaging shows that the Al<sub>2</sub>O<sub>3</sub>rich film/substrate interface forms extended porous areas after irradiation, most likely due to radiation hardening and crystallization processes. These porous areas between the UO<sub>2</sub> film and the substrate considerably limit the diffusion of Mg. Future works should explore the effects of more extended irradiation and heating on structural changes of thin films.

#### 5. Conclusions

This work reports a spraying-assisted SCS preparation method of high-quality polycrystalline UO2 thin films on Al alloy substrates. The process allows the deposition of uniform films without any material loss, thus making spraying-assisted SCS ideal for fabricating thin films of highly radioactive oxides. This method can be used for the efficient preparation of transuranic elements with limited quantities of source materials. High-resolution TEM measurements and layer-by-layer XPS analysis demonstrated that increasing the annealing temperatures or times facilitate the diffusion of Mg from the alloy into the UO2, decreasing the overall crystallinity of the films. The prepared films do not undergo material losses during high-energy ion irradiation. However, the Mg content significantly influences irradiation-induced restructuring of the UO2 films. Irradiated films with low (or no) Mg content exhibit reduced porosity and improved crystallinity, while the UO<sub>2</sub>/Al interfacial layer becomes highly porous. Films with higher Mg content are mostly amorphized after irradiation, while the substrate/ film interfaces experience only minor changes. The origin of irradiationinduced amorphization is related to the Mg diffusion and subsequent formation of Mg<sub>v</sub>U<sub>1-v</sub>O<sub>2+x</sub> solid solutions. Chemically complex, porefree, and amorphous Mg-Al-O film/substrates with interfacial layers enable continuous diffusion of Mg during irradiation. Gradual increase in Mg amounts triggers irradiation-induced precipitation of a crystalline MgO-rich phase within the amorphous films.

#### CRediT authorship contribution statement

**Stefania Dede:** Investigation, Formal analysis, Writing – original draft. **Khachatur V. Manukyan:** Conceptualization, Methodology, Supervision, Funding acquisition. **Jordan M. Roach:** Investigation. **Ashabari Majumdar:** Investigation. **Peter C. Burns:** Writing – review & editing, Supervision. **Ani Aprahamian:** Writing – review & editing, Supervision, Funding acquisition.

#### **Declaration of Competing Interest**

The authors declare that they have no known competing financial interests or personal relationships that could have appeared to influence the work reported in this paper.

#### Data availability

No data was used for the research described in the article.

#### Acknowledgments

The work was performed with financial support in part from the U.S. Department of Energy's (DOE) National Nuclear Security Administration (NNSA, Grant # DE-NA0003888), U.S. National Science Foundation (NSF, PHY-2011890), and JINA-CEE NSF Physics Frontiers Centers (Award #1430152). A.A. acknowledges support from the Fulbright U.S. Scholar grant. K.M. also acknowledges funding from the U.S. Army Research Office Grant # W911NF2110045 under the Materials Synthesis & Processing Program, with Dr. Michael P. Bakas as the program manager. The authors also acknowledge Notre Dame Center for Environmental Science & Technology (CEST), Materials Characterization Facility (MCF), and Integrated Imaging Facility (NDIIF) for instrumental usage.

#### Appendix A. Supplementary material

Supplementary data to this article can be found online at https://doi.org/10.1016/j.apsusc.2022.154437.

#### References

- P.C. Burns, R.C. Ewing, A. Navrotsky, Nuclear fuel in a reactor accident, Science 335 (6073) (2012) 1184–1188.
- [2] L. Desgranges, G. Baldinozzi, G. Rousseau, J.C. Nièpce, G. Calvarin, Neutron diffraction study of the in situ oxidation of UO2, Inorg. Chem. 48 (2009) 7585–7592, https://doi.org/10.1021/ic9000889.
- [3] C. Lovis, X. Dumusque, N.C. Santos, F. Bouchy, M. Mayor, F. Pepe, D. Queloz, D. Ségransan, S. Udry, The HARPS search for southern extra-solar planets. XXXI. Magnetic activity cycles in solar-type stars: statistics and impact on precise radial velocities 346 (2011) 984–987.
- [4] K.O. Kvashnina, S.M. Butorin, P. Martin, P. Glatzel, Chemical state of complex uranium oxides, Phys. Rev. Lett. 111 (2013) 1–5, https://doi.org/10.1103/ PhysRevLett.111.253002.
- [5] K. Gofryk, S. Du, C.R. Stanek, J.C. Lashley, X.Y. Liu, R.K. Schulze, J.L. Smith, D. J. Safarik, D.D. Byler, K.J. McClellan, B.P. Uberuaga, B.L. Scott, D.A. Andersson, Anisotropic thermal conductivity in uranium dioxide, Nat. Commun. 5 (2014) 1–7, https://doi.org/10.1038/ncomms5551.
- [6] L. Desgranges, Y. Ma, P. Garcia, G. Baldinozzi, D. Siméone, H.E. Fischer, What is the actual local crystalline structure of uranium dioxide, UO2? A new perspective for the most used nuclear fuel, Inorg. Chem. 56 (2017) 321–326, https://doi.org/ 10.1021/acs.inorgchem.6b02111.
- [7] K.I. Maslakov, Y.A. Teterin, A.J. Popel, A.Y. Teterin, K.E. Ivanov, S.N. Kalmykov, V. G. Petrov, R. Springell, T.B. Scott, I. Farnan, XPS study of the surface chemistry of UO2 (111) single crystal film, Appl. Surf. Sci. 433 (2018) 582–588, https://doi.org/10.1016/J.APSUSC.2017.10.019.
- [8] V.V. Rondinella, T. Wiss, The high burn-up structure in nuclear fuel, Mater. Today. 13 (2010) 24–32, https://doi.org/10.1016/S1369-7021(10)70221-2.
- [9] N. Capps, C. Jensen, F. Cappia, J. Harp, K. Terrani, N. Woolstenhulme, D. Wachs, A critical review of high burnup fuel fragmentation, relocation, and dispersal under loss-of-coolant accident conditions, J. Nucl. Mater. 546 (2021), 152750, https:// doi.org/10.1016/j.jnucmat.2020.152750.
- [10] J. Rest, M.W.D. Cooper, J. Spino, J.A. Turnbull, P. Van Uffelen, C.T. Walker, Fission gas release from UO2 nuclear fuel: A review, J. Nucl. Mater. 513 (2019) 310–345, https://doi.org/10.1016/j.jnucmat.2018.08.019.
- [11] H. Idriss, Surface reactions of uranium oxide powder, thin films and single crystals, Surf. Sci. Rep. 65 (2010) 67–109, https://doi.org/10.1016/j.surfrep.2010.01.001.
- [12] Y. Miao, T. Yao, J. Lian, J.S. Park, J. Almer, S. Bhattacharya, A.M. Yacout, K. Mo, In situ synchrotron investigation of grain growth behavior of nano-grained UO2, Scr. Mater. 131 (2017) 29–32, https://doi.org/10.1016/j.scriptamat.2016.12.025.
- [13] H. Matzke, L.M. Wang, High-resolution transmission electron microscopy of ion irradiated uranium oxide, J. Nucl. Mater. 231 (1996) 155–158, https://doi.org/ 10.1016/0022-3115(96)00369-8.
- [14] T.J. Gerczak, C.M. Parish, P.D. Edmondson, C.A. Baldwin, K.A. Terrani, Restructuring in high burnup UO2 studied using modern electron microscopy, J. Nucl. Mater. 509 (2018) 245–259, https://doi.org/10.1016/j. inucmat.2018.05.077.
- [15] Y. Miao, T. Yao, J. Lian, S. Zhu, S. Bhattacharya, A. Oaks, A.M. Yacout, K. Mo, Nano-crystallization induced by high-energy heavy ion irradiation in UO2, Scr. Mater. 155 (2018) 169–174, https://doi.org/10.1016/j.scriptamat.2018.04.006.
- [16] C. McKinney, R. Seibert, G. Helmreich, A. Aitkaliyeva, K. Terrani, Three-dimensional bubble reconstruction in high burnup UO2, J. Nucl. Mater. 532 (2020), 152053, https://doi.org/10.1016/j.jnucmat.2020.152053.

- [17] I. Zacharie-Aubrun, R. Henry, T. Blay, L. Brunaud, J.M. Gatt, J. Noirot, S. Meille, Effects of irradiation on mechanical properties of nuclear UO2 fuels evaluated by Vickers indentation at room temperature, J. Nucl. Mater. 547 (2021), 152821, https://doi.org/10.1016/j.jnucmat.2021.152821.
- [18] M. Bricout, C. Onofri, A. Debelle, Y. Pipon, R.C. Belin, F. Garrido, F. Leprêtre, G. Gutierrez, Radiation damage in uranium dioxide: Coupled effect between electronic and nuclear energy losses, J. Nucl. Mater. 531 (2020) 151967.
- [19] L. Van Brutzel, E. Vincent-Aublant, J.-M. Delaye, Large molecular dynamics simulations of collision cascades in single-crystal, bi-crystal, and poly-crystal UO2, Nucl. Instrum. Methods Phys. Res. Sect. B Beam Interact. Mater. Atoms. 267 (18) (2009) 3013–3016.
- [20] J. Rest, G.L. Hofman, Dynamics of irradiation-induced grain subdivision and swelling in U3Si2 and UO2 fuels, J. Nucl. Mater. 210 (1994) 187–202, https://doi. org/10.1016/0022-3115(94)90237-2.
- [21] J. Rest, A model for the effect of the progression of irradiation-induced recrystallization from initiation to completion on swelling of UO2 and U-10Mo nuclear fuels, J. Nucl. Mater. 346 (2005) 226–232, https://doi.org/10.1016/j. inucryst 2005 06 012
- [22] C. Onofri, M. Legros, J. Léchelle, H. Palancher, C. Baumier, C. Bachelet, C. Sabathier, Full characterization of dislocations in ion-irradiated polycrystalline UO2, J. Nucl. Mater. 494 (2017) 252–259, https://doi.org/10.1016/j. inucmat.2017.07.043.
- [23] L. Van Brutzel, M. Rarivomanantsoa, Molecular dynamics simulation study of primary damage in UO2 produced by cascade overlaps, J. Nucl. Mater. 358 (2006) 209–216, https://doi.org/10.1016/j.jnucmat.2006.07.009.
- [24] G. Sattonnay, L. Vincent, F. Garrido, L. Thomé, Xenon versus helium behavior in UO2 single crystals: A TEM investigation, J. Nucl. Mater. 355 (2006) 131–135, https://doi.org/10.1016/j.jnucmat.2006.04.013.
- [25] R. Parrish, A. Winston, J. Harp, A. Aitkaliyeva, TEM characterization of high burnup fast-reactor MOX fuel, J. Nucl. Mater. 527 (2019) 151794.
- [26] H. Matzke, A. Turos, G. Linker, Polygonization of single crystals of the fluorite-type oxide UO2 due to high dose ion implantation +, Nucl. Inst. Methods Phys. Res. B. 91 (1994) 294–300, https://doi.org/10.1016/0168-583X(94)96234-0.
- [27] M.G. Abdoelatef, F. Badry, D. Schwen, C. Permann, Y. Zhang, K. Ahmed, Mesoscale modeling of high burn-up structure formation and evolution in UO2, JOM. 71 (2019) 4817–4828, https://doi.org/10.1007/s11837-019-03830-z.
- [28] A.J. Popel, A.M. Adamska, P.G. Martin, O.D. Payton, G.I. Lampronti, L. Picco, L. Payne, R. Springell, T.B. Scott, I. Monnet, C. Grygiel, I. Farnan, Structural effects in UO2 thin films irradiated with U ions, Nucl. Instrum. Methods Phys. Res. Sect. B Beam Interact. Mater. Atoms. 386 (2016) 8–15, https://doi.org/10.1016/j.nimb.2016.09.019.
- [29] S.C. Middleburgh, W.E. Lee, M.J.D. Rushton, Structure and properties of amorphous uranium dioxide, Acta Mater. 202 (2021) 366–375, https://doi.org/ 10.1016/j.actamat.2020.10.069.
- [30] P. Sapkota, A. Aprahamian, K.Y. Chan, B. Frentz, K.T. Macon, S. Ptasinska, D. Robertson, K. Manukyan, Irradiation-induced reactions at the CeO2/SiO2/Si interface, J. Chem. Phys. 152 (10) (2020) 104704.
- [31] Y.A. Teterin, A.J. Popel, K.I. Maslakov, A.Y. Teterin, K.E. Ivanov, S.N. Kalmykov, R. Springell, T.B. Scott, I. Farnan, XPS Study of Ion Irradiated and Unirradiated UO2 Thin Films, Inorg. Chem. 55 (2016) 8059–8070, https://doi.org/10.1021/acs. inorgchem.6b01184.
- [32] M.S. Elbakhshwan, Y. Miao, J.F. Stubbins, B.J. Heuser, Mechanical properties of UO2 thin films under heavy ion irradiation using nanoindentation and finite element modeling, J. Nucl. Mater. 479 (2016) 548–558, https://doi.org/10.1016/j.imjurnat.2016.07.047
- [33] K.I. Maslakov, Y.A. Teterin, A.J. Popel, A.Y. Teterin, K.E. Ivanov, S.N. Kalmykov, V. G. Petrov, P.K. Petrov, I. Farnan, XPS study of ion irradiated and unirradiated CeO 2 bulk and thin film samples, Appl. Surf. Sci. 448 (2018) 154–162, https://doi.org/10.1016/j.apsusc.2018.04.077.
- [34] A.J. Popel, V.G. Petrov, V.A. Lebedev, J. Day, S.N. Kalmykov, R. Springell, T. B. Scott, I. Farnan, The effect of fission-energy Xe ion irradiation on dissolution of UO2 thin films, J. Alloys Compd. 721 (2017) 586–592, https://doi.org/10.1016/j.iallcom.2017.05.084.
- [35] P. Bera, Solution Combustion Synthesis as a Novel Route to Preparation of Catalysts, Int. J. Self-Propagating High-Temp. Synth. 282 (28) (2019) 77–109, https://doi.org/10.3103/S106138621902002X.
- [36] N. Amirkhanyan, S. Kharatyan, K. Manukyan, A. Aprahamian, Thermodynamics and kinetics of solution combustion synthesis: Ni(NO3)2 + fuels systems, Combust. Flame. 221 (2020) 110–119, https://doi.org/10.1016/j. combustflame.2020.07.038.
- [37] A.S. Mukasyan, S. Roslyakov, J.M. Pauls, L.C. Gallington, T. Orlova, X. Liu, M. Dobrowolska, J.K. Furdyna, K.V. Manukyan, Nanoscale Metastable ε-Fe3N Ferromagnetic Materials by Self-Sustained Reactions, Inorg. Chem. 58 (2019) 5583–5592, https://doi.org/10.1021/acs.inorgchem.8b03553.
- [38] E. Carlos, R. Martins, E. Fortunato, R. Branquinho, Solution combustion synthesis: towards a sustainable approach for metal oxides, Chem. - A Eur. J. 26 (2020) 9099–9125, https://doi.org/10.1002/chem.202000678.
- [39] B. Wang, P. Guo, L. Zeng, X. Yu, A. Sil, W. Huang, M.J. Leonardi, X. Zhang, G. Wang, S. Lu, Z. Chen, M.J. Bedzyk, R.D. Schaller, T.J. Marks, A. Facchetti, Expeditious, scalable solution growth of metal oxide films by combustion blade coating for flexible electronics, Proc. Natl. Acad. Sci. U. S. A. 116 (2019) 9230–9238, https://doi.org/10.1073/pnas.1901.492116.
- [40] K. Rajeshwar, N.R. de Tacconi, Solution combustion synthesis of oxide semiconductors for solar energy conversion and environmental remediation, Chem. Soc. Rev. 38 (2009) 1984–1998, https://doi.org/10.1039/b811238j.

- [41] B. Wang, W. Huang, M.J. Bedzyk, V.P. Dravid, Y.-Y. Hu, T.J. Marks, A. Facchetti, Combustion synthesis and polymer doping of metal oxides for high-performance electronic circuitry, Acc. Chem. Res. 55 (2022) 429–441, https://doi.org/10.1021/ acs.accounts.1c00671.
- [42] P. Bera, M.S. Hegde, Noble metal ions in CeO2 and TiO2: synthesis, structure and catalytic properties, RSC Adv. 5 (2015) 94949–94979, https://doi.org/10.1039/ C5R416474F
- [43] M.K. Hossain, H.P. Sarker, P. Sotelo, U. Dang, I. Rodríguez-Gutiérrez, J. Blawat, A. Vali, W. Xie, G. Oskam, M.N. Huda, R.T. MacAluso, K. Rajeshwar, Phase-Pure Copper Vanadate (α-CuV2O6): Solution Combustion Synthesis and Characterization, Chem. Mater. 32 (2020) 6247–6255, https://doi.org/10.1021/ ACS.CHEMMATER.0C02227/SUPPL\_FILE/CM0C02227\_SI\_001.PDF.
- [44] J.M. Roach, K.V. Manukyan, A. Majumdar, S. Dede, A.G. Oliver, P.C. Burns, A. Aprahamian, Hyperstoichiometric uranium dioxides: rapid synthesis and irradiation-induced structural changes, Inorg. Chem. 60 (2021) 18938–18949, https://doi.org/10.1021/acs.inorgchem.1c02736.
- [45] A. Majumdar, K.V. Manukyan, S. Dede, J.M. Roach, D. Robertson, P.C. Burns, A. Aprahamian, Irradiation-driven restructuring of UO2 thin films: amorphization and crystallization, ACS Appl. Mater. Interfaces. 13 (2021) 35153–35164, https://doi.org/10.1021/ACSAMI.1C08682/SUPPL\_FILE/AM1C08682\_SI\_001.PDF.
- [46] D.A. Shirley, High-resolution X-ray photoemission spectrum of the valence bands of gold, Phys. Rev. B. 5 (12) (1972) 4709–4714.
- [47] F. Neal, C.S. Ltd., CasaXPS processing software for XPS spectra, Casa Software Ltd., 2009.
- [48] V.I. Nefedov, X-ray electron spectroscopy of chemical compounds, 1984. https://doi.org/10.3/JQUERY-UI.JS.
- [49] I.M. Band, Y.I. Kharitonov, M.B. Trzhaskovskaya, Photoionization cross sections and photoelectron angular distributions for x-ray line energies in the range 0.132–4.509 keV targets:  $1 \le Z \le 100$ , At. Data Nucl. Data Tables. 23 (1979) 443–505, https://doi.org/10.1016/0092-640X(79)90027-5.
- [50] Y.A. Teterin, K.I. Maslakov, M. V Ryzhkov, O.A. Trapari, L. Vuk V Cevi, A.Y. Teterin, A.D. Panov, Translated from Radiokhimiya, Radiochemistry 47 (2005) 193–202.
- [51] K. Manukyan, C. Fasano, A. Majumdar, G.F. Peaslee, M. Raddell, E. Stech, M. Wiescher, Surface manipulation techniques of Roman denarii, Appl. Surf. Sci. 493 (2019) 818–828, https://doi.org/10.1016/J.APSUSC.2019.06.296.
- [52] K.V. Manukyan, Y.C. Lin, S. Rouvimov, P.J. McGinn, A.S. Mukasyan, Microstructure-reactivity relationship of Ti + C reactive nanomaterials, J. Appl. Phys. 113 (2013), 024302, https://doi.org/10.1063/1.4773475.
- [53] E.S. Ilton, P.S. Bagus, XPS determination of uranium oxidation states, Surf. Interface Anal. 43 (2011) 1549–1560, https://doi.org/10.1002/sia.3836.
- [54] A.K. Burrell, T.M. McCleskey, P. Shukla, H. Wang, T. Durakiewicz, D.P. Moore, C. G. Olson, J.J. Joyce, Q. Jia, Controlling oxidation states in uranium oxides through epitaxial stabilization, Adv. Mater. 19 (2007) 3559–3563, https://doi.org/10.1002/ADMA.200701157.
- [55] M.S. Elbakhshwan, B.J. Heuser, Structural and compositional characterization of single crystal uranium dioxide thin films deposited on different substrates, Thin Solid Films 636 (2017) 658–663, https://doi.org/10.1016/J.TSF.2017.07.020.
- [56] B.L. Scott, J.J. Joyce, T.D. Durakiewicz, R.L. Martin, T.M. McCleskey, E. Bauer, H. Luo, Q. Jia, High quality epitaxial thin films of actinide oxides, carbides, and nitrides: Advancing understanding of electronic structure of f-element materials, Coord. Chem. Rev. 266–267 (2014) 137–154, https://doi.org/10.1016/j. ccr.2013.09.019.
- [57] H. Wendeler, R. Deissenberger, F.J. Urban, N. Trautmann, G. Herrmann, Electrolytic preparation of actinide filaments for laser resonance ionization spectroscopy, Nucl. Inst. Methods Phys. Res. A. 334 (1993) 93–95, https://doi.org/ 10.1016/0168-9002(93)90532-M.
- [58] J.P. Greene, I. Ahmad, Molecular plating of actinides on thin backings, Nucl. Instrum. Methods Phys. Res. Sect. A Accel. Spectrometers, Detect. Assoc. Equip. 590 (2008) 131–133, https://doi.org/10.1016/j.nima.2008.02.076.
- [59] S. Sadi, A. Paulenova, P.R. Watson, W. Loveland, Growth and surface morphology of uranium films during molecular plating, Nucl. Instrum. Methods Phys. Res. Sect. A Accel. Spectrometers, Detect. Assoc. Equip. 655 (2011) 80–84, https://doi.org/ 10.1016/j.nima.2011.06.025.
- [60] K. Eberhardt, C.E. Düllmann, R. Haas, C. Mokry, J. Runke, P. Thörle-Pospiech, N. Trautmann, Actinide targets for fundamental research in nuclear physics, in: AIP Conf. Proc., 2018. https://doi.org/10.1063/1.5035526.
- [61] Q. Chen, X. Lai, B. Bai, M. Chu, Structural characterization and optical properties of UO 2 thin films by magnetron sputtering, Appl. Surf. Sci. 256 (2010) 3047–3050, https://doi.org/10.1016/j.apsusc.2009.11.071.
- [62] J. Lin, I. Dahan, B. Valderrama, M.V. Manuel, Structure and properties of uranium oxide thin films deposited by pulsed dc magnetron sputtering, Appl. Surf. Sci. 301 (2014) 475–480, https://doi.org/10.1016/j.apsusc.2014.02.106.
- [63] S. Rennie, E. Lawrence Bright, J.E. Sutcliffe, J.E. Darnbrough, R. Burrows, J. Rawle, C. Nicklin, G.H. Lander, R. Springell, The role of crystal orientation in the dissolution of UO2 thin films, Corros. Sci. 145 (2018) 162–169, https://doi.org/ 10.1016/j.corsci.2018.09.012.
- [64] A.J. Popel, S.R. Spurgeon, B. Matthews, M.J. Olszta, B.T. Tan, T. Gouder, R. Eloirdi, E.C. Buck, I. Farnan, An Atomic-Scale Understanding of UO2Surface Evolution during Anoxic Dissolution, ACS Appl. Mater. Interfaces. 12 (2020) 39781–39786, https://doi.org/10.1021/acsami.0c09611.
- [65] S. Rennie, E. Lawrence Bright, J.E. Darnbrough, L. Paolasini, A. Bosak, A.D. Smith, N. Mason, G.H. Lander, R. Springell, Study of phonons in irradiated epitaxial thin films of UO2, Phys. Rev. B. 97 (2018) 1–9, https://doi.org/10.1103/ PhysRevB.97.224303.

- [66] L. Appel, J. Leduc, C.L. Webster, J.W. Ziller, W.J. Evans, S. Mathur, Synthesis of Air-Stable, Volatile Uranium(IV) and (VI) Compounds and Their Gas-Phase Conversion To Uranium Oxide Films, Angew Chemie. 127 (2015) 2237–2241, https://doi.org/10.1002/ange.201409606.
- [67] M.D. Straub, J. Leduc, M. Frank, A. Raauf, T.D. Lohrey, S.G. Minasian, S. Mathur, J. Arnold, Chemical Vapor Deposition of Phase-Pure Uranium Dioxide Thin Films from Uranium(IV) Amidate Precursors, Angew. Chemie - Int. Ed. 58 (2019) 5749–5753, https://doi.org/10.1002/anie.201901924.
- [68] Y. Shiokawa, R. Amano, A. Nomura, M. Yagi, Preparation of lanthanide, thorium and uranium oxide films by chemical vapor deposition using β-diketone chelates, J. Radioanal. Nucl. Chem. Artic. 152 (1991) 373–380, https://doi.org/10.1007/ BF02104690.
- [69] T. Fujino, K. Naito, Studies on cubic magnesium uranate, MgyU1-yO2+x-I. Phase relations and crystal chemistry, J. Inorg. Nucl. Chem. 32 (1970) 627–636, https://doi.org/10.1016/0022-1902(70)80273-1.
- [70] T. Fujino, S. Nakama, N. Sato, K. Yamada, K. Fukuda, H. Serizawa, T. Shiratori, Solubility of magnesium in uranium dioxide Takeo, J. Nucl. Mater. 246 (2-3) (1997) 150–157.
- [71] T. Fujino, N. Sato, K. Yamada, S. Nakama, K. Fukuda, H. Serizawa, T. Shiratori, Thermodynamics of the UO2 solid solution with magnesium and europium oxides, J. Nucl. Mater. 297 (2001) 332–340, https://doi.org/10.1016/S0022-3115(01) 00627-4.
- [72] T. Fujino, T. Shiratori, N. Sato, K. Fukuda, K. Yamada, H. Serizawa, Post-irradiation examination of high burnup Mg doped UO2 in comparison with undoped UO2, Mg-Nb doped UO2 and Ti doped UO2, J. Nucl. Mater. 297 (2001) 176–205, https:// doi.org/10.1016/S0022-3115(01)00609-2.